PHYSICAL REVIEW B **89**, 174423 (2014)

Long-range and short-range magnetic order in the singlet ground state system $TbCo_3B_2$

Oleg Rivin[*,†]
Department of Physics, Nuclear Research Centre–Negev, P.O. Box 9001, Beer Sheva 84190, Israel
and Department of Physics, Ben-Gurion University, P.O. Box 653, Beer Sheva 84105, Israel

Hagai Shaked
Department of Physics, Ben-Gurion University, P.O. Box 653, Beer Sheva 84105, Israel

Arsen Gukasov
Laboratoire Léon Brillouin, CEA-CNRS, CE Saclay, 91191 Gif sur Yvette, France

El'ad N. Caspi
Department of Physics, Nuclear Research Centre–Negev, P.O. Box 9001, Beer Sheva 84190, Israel

(Received 20 March 2014; revised manuscript received 28 April 2014; published 20 May 2014)

The YCo_3B_2 compound is studied by polarized neutron powder diffraction in search of magnetic order. It is found that YCo_3B_2 remains paramagnetic down to 10 K. Neutron powder diffraction study of the induced transition in the Van Vleck paramagnet $TbCo_3B_2$ revealed a significant contribution of magnetic diffuse scattering at small angles and near the (100) reflection. Analysis of these results leads to a revised magnetic structure of $TbCo_3B_2$, in which the Tb sublattice orders ferromagnetically at 31 K, with no Co ordering. Also, short-range magnetic order of the Tb sublattice, extending into the paramagnetic region, was found. The temperature evolution of this short-range order's correlation length, in the paramagnetic temperatures region, shows a significant anomaly unique to induced transition magnetic ordering.

DOI: 10.1103/PhysRevB.89.174423 PACS number(s): 75.25.−j, 75.40.−s

I. INTRODUCTION

The RCo_3B_2 ($R =$ lanthanides) materials are of hexagonal symmetry ($P6/mmm$ [1]) and are derived from the RCo_5 by substitution of B for the Co at the $2c$ [1] site (Fig. 1) [2]. The magnetic ordering temperatures [3–6] of the RCo_3B_2 (<60 K) are significantly lower than those found [7] in the RCo_5 (∼1000 K). The R sublattice in RCo_3B_2 orders ferromagnetically, with reduced magnitude of the ordered magnetic moment compared to RCo_5 (approximate free ion value) [3,4,8]. These properties were found [8] to be strongly controlled by the crystalline electric field (CEF) and magnetic exchange field (MEF) in these materials, which have been extensively studied theoretically and experimentally for many years [3–10].

The Tb sublattice in $TbCo_3B_2$ was reported [3] to undergo a transition to ferromagnetic order at T_{Tb} ∼31 K. Later, it was shown [8] that the CEF-only ground state of the Tb ions is a nonmagnetic singlet, and the magnetic ordering transition is an induced transition [11–13]. In an induced magnetic transition, magnetic moment is induced into the singlet ground state by a component of the MEF, perpendicular to the CEF, which admixes higher lying states into the singlet ground state via a mechanism similar to the Van Vleck susceptibility. The induced moment causes the MEF to increase, in turn causing the induced moment to increase, until order sets in through a bootstraplike process. This is different from conventional magnetic ordering in which order emerges through alignment, by MEF, of constant paramagnetic moments μ_{eff}. The CEF and the MEF on the Tb $1a$ site were reported [8] to be parallel and perpendicular to the hexagonal c axis, respectively.

The magnetic state of the Co sublattice in RCo_3B_2 (the $3g$ site, Fig. 1) and its role in the magnetic ordering process were subject to some controversy in the past. Previously, magnetic ordering temperature was proposed to be ∼170 K, at which an unexplained susceptibility increase was observed [3,8]. A Co magnetic moment of ∼0.1 μ_B along the c axis was reported in a neutron powder diffraction (NPD) study of $TbCo_3B_2$ [3].

Above T_{Tb}, NPD showed a neutron count in excess of that contributed by the crystal lattice (i.e., nuclear scattering) at several Bragg reflections positions [3]. We now recognize that this excess count appears as broadened Bragg reflections. Previously [3], this broadening was overlooked, and in the application of the Rietveld refinement method, this excess neutron count was included as magnetic Bragg scattering. The magnetic ordering above T_{Tb} was proposed to be induced by a MEF generated by the previously mentioned ordered Co sublattice. However, several results are inconsistent with ordering of the Co sublattice in RCo_3B_2. First, the theoretical model and the induced transitions theory of the Tb sublattice exclude interaction with other sublattices [8,13]. Second, an inelastic neutron scattering experiment revealed no change in the magnetic state of the Tb sublattice from 200 to 40 K [8], whereas an ordering of the Co sublattice at 170 K would have introduced such a change. Third, magnetization measurements [6] performed on YCo_3B_2, in which the Tb^{3+} ions were replaced by the nonmagnetic Y^{3+}, revealed little or no magnetic response. Fourth, theoretical calculations did not find a possibility for sustainable ferromagnetic Co ordering in YCo_3B_2 [9]. Moreover, it was suggested [14] that the observed susceptibility change ∼170 K, in $TbCo_3B_2$ and YCo_3B_2,

---

[*] Corresponding author: lexoed@gmail.com and rivino@bgu.ac.il

[†] Present address: Department of Physics, Nuclear Research Centre-Negev, P.O. Box 9001, Beer Sheva 84190, Israel.

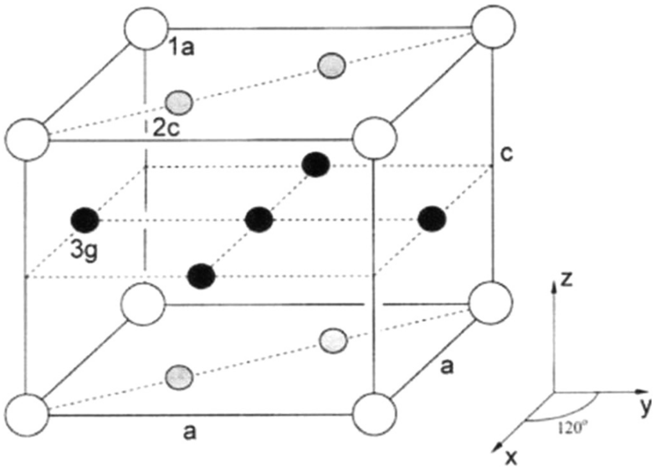

FIG. 1. The CaCu$_5$-type crystallographic structure of RCo$_3$B$_2$, in which the R, Co, and B ions occupy the $1a$ ($6/mmm$), $3g$ (mmm), and $2c$ ($\bar{6}m2$) sites, respectively.

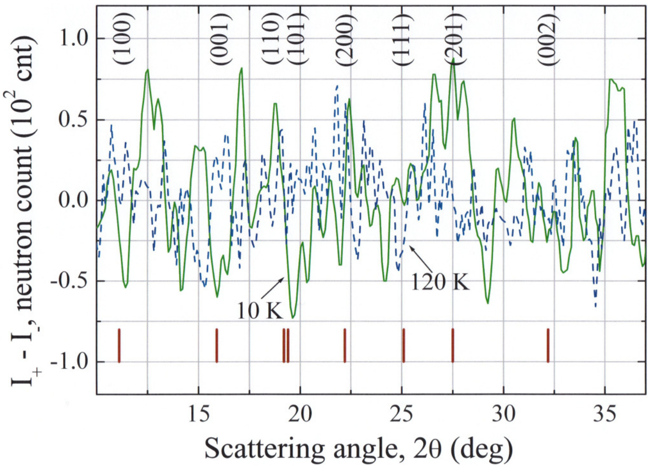

FIG. 2. (Color online) FD, $I_+ - I_-$, profile of YCo$_3$B$_2$ at 10 K (solid line) and 120 K (dashed line). The expected 2θ positions of the Bragg reflections are marked below, and their hexagonal ($P6/mmm$) Miller indices are given above.

originates from an itinerant response with no Co long-range order (LRO). Finally, the reported [3] low-temperature orientation of the ferrimagnetic (including Co LRO) axis in TbCo$_3$B$_2$ was 74(2)° with respect to the hexagonal c axis, whereas theoretical calculation of the magnetic anisotropy predicted that the magnetic axis is oriented in the hexagonal plane, perpendicular to the c axis [8], suggesting a systematic error in the reported [3] model that includes LRO on the Co sublattice.

In the present paper, a study in search of a magnetically ordered Co sublattice in YCo$_3$B$_2$ is carried out using polarized neutron powder diffraction (PNPD). Next, we revisit TbCo$_3$B$_2$, by adding to the analysis the contribution of the excess broadened count as magnetic diffuse scattering (MDS). The results of these two show an absence of Co LRO in YCo$_3$B$_2$ and emergence (above T_{Tb}) of a Tb magnetic short-range order (SRO) with no Co ordering in TbCo$_3$B$_2$.

II. EXPERIMENTS AND RESULTS

A. YCo$_3$B$_2$ PNPD study

Polycrystalline YCo$_3{}^{11}$B$_2$ was prepared in an arc melting furnace using high purity elements (99.9%). We use here the previously prepared sample; its processing and characterization are described in detail in Ref. [5].

Polarized neutron powder diffraction experiments were performed at 10 and 120 K. The measurements were carried out at the very intense polarized (VIP, former 5C1) diffractometer [15,16] at the Orpheé research reactor in the Laboratoire Léon Brillouin, Centre d'Etudes Atomiques–Centre National de la Recherche Scientifique, Saclay, France. A monochromatic [$\lambda = 0.84(1)$ Å] and polarized [$P = 0.88(1)$] incident neutron beam was obtained using the Heusler crystal (Cu$_2$MnAl) method [17]. A cryoflipper, installed between the Heusler crystal and the sample, was used for the neutron spin reversal with respect to the externally applied magnetic field, H_0, perpendicular to the scattering plane in the up (+) direction. The scattered neutrons were detected using a two-dimensional (2D) position sensitive ^{3}He detector, limiting the measured neutrons to a vertical acceptance angle of −5° to 5° about the scattering plane. A 10.0(1) g YCo$_3{}^{11}$B$_2$ powder sample was loaded into a Ti$_{0.522}$Zr$_{0.478}$ (Ti/Zr) cylindrical sample holder, with a 5 mm diameter and ~0.2 mm wall thickness. This (Ti/Zr) holder was used to reduce possible coherent scattering from the holder [18]. The loaded sample holder was placed in the aforementioned external magnetic field, H_0, of 5.75 T to achieve saturation magnetization (if exists), at different sample temperatures. The PNPD experiment yields the observed neutron counts, I_+ and I_-, at scattering angle 2θ with the incident neutron beam polarized parallel and antiparallel to the external magnetic field direction, respectively. In practice, these counts are represented by the neutron count collected per 2θ channel per prefixed beam monitor counts.

The PNPD flipping difference (FD) neutron count: $I_+ - I_-$, was shown [16,19,20] to eliminate all nonmagnetic scattering (i.e., nuclear scattering, scattering from the cryomagnet, multiple, or diffuse, scattering, and constant background), enhancing sensitivity to magnetic scattering contribution from small ordered magnetic moments compared with NPD.

The 2θ positions of the Bragg reflections (Fig. 2), were calculated using the hexagonal lattice parameters: $a_0 = 5.04(1)$ and $c_0 = 3.03(1)$ Å [5]. Above 2θ ~35° (not shown), the angular resolution of the VIP diffractometer becomes too poor (full width at half-maximum > 3.5°) [16]. No Bragg reflections are present below 10°. Clearly, the observed YCo$_3$B$_2$ FD profile (Fig. 2) does not reveal any excess neutron count, above statistical variation, in the vicinity of the Bragg positions at either 120 or 10 K.

B. TbCo$_3$B$_2$ NPD study

The experimental data used in this section were collected at the high-resolution powder thermal (HRPT) neutron diffractometer at the Paul Scherrer Institute (Switzerland), described in a previous paper on TbCo$_3{}^{11}$B$_2$ [3].

Examination of the neutron count of the (100) reflection at 39.4(1) K $> T_{\mathrm{Tb}}$, [Fig. 3(a)] reveals that (i) the (full profile) refined contribution (solid line) significantly exceeds

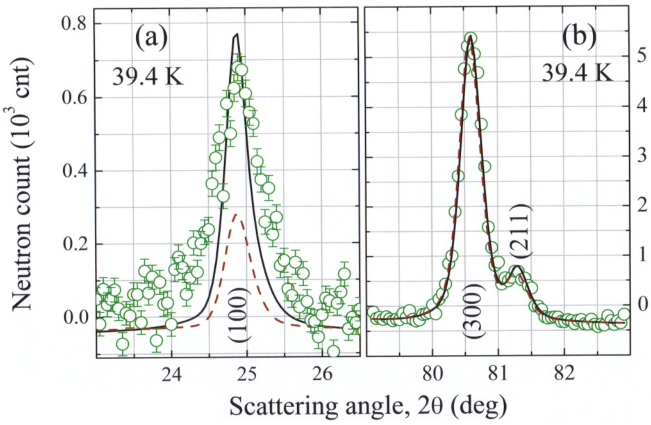

FIG. 3. (Color online) Two sections of the observed (circles) and Rietveld (solid line) NPD profiles of $TbCo_3B_2$ at 39.4(1) K. The Rietveld profile was calculated using nuclear (dashed line) and magnetic LRO components. (a) The observed profile of the (100) reflection has large magnetic contribution and is significantly broader than the Rietveld line width. (b) The observed profile of the (300, 211) reflections has practically no magnetic contribution and shows no broadening compared to the Rietveld line widths. The error bars in (b) are smaller than the symbol's size.

the refined nuclear (dashed line) contribution due to magnetic contribution; and (ii) the observed (100) profile is significantly broadened compared to the refined width (solid line) and the observed (300) width [Fig. 3(b)], which is dominated by a nuclear contribution. The previously proposed contribution from magnetic LRO on the Tb sublattice (Sec. III B 1), does not account for the broadened line profile of the (100) reflection [Fig. 3(a)]. Similar profile broadening is observed in the (102) reflection (not shown), which is also dominated by magnetic contribution.

The temperature evolution of the observed (100) profile at the paramagnetic temperatures region is shown in Fig. 4. This temperature-dependent broadening constitutes MDS and can be accounted for by magnetic SRO.

Observed temperature evolutions of the neutron count at $2\theta = 15°$ [Fig. 5(a)] and at 5° [Fig. 5(b)] are shown. The 5° count includes the contribution of MDS to small scattering angles, in addition to that found in the vicinity of Bragg reflections. The 15° count reveals the contribution of other scattering process to the 5° count, because at this angle the magnetic form factor remains constant (Sec. III B 4). The temperature evolution of the neutron count, obtained after subtraction of the 15° count from the 5° count, exhibits a "critical scattering"-like [20] behavior, which also indicates the emergence of SRO.

III. ANALYSIS

A. YCo_3B_2 PNPD

1. Statistical noise analysis

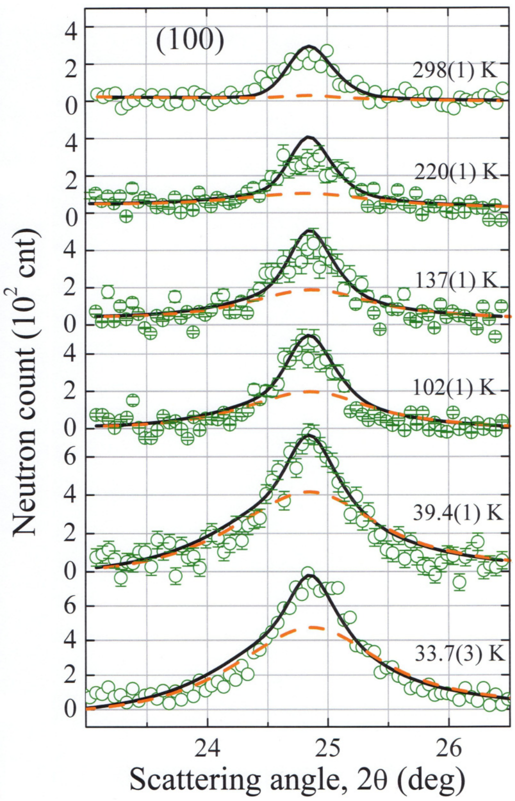

FIG. 4. (Color online) The temperature evolution of the observed (circles) and Rietveld refined (solid line) (100) profile at various temperatures in the paramagnetic temperatures region. The refined profile is obtained using nuclear LRO, magnetic LRO, and magnetic SRO (dashed line) components (Sec. III B). An appropriate background was subtracted from the observed and refined profiles for display purposes. If not shown, the error bars are smaller than the symbol's size.

The possible presence of small Bragg reflections is examined using analysis of the statistical variations in the observed FD profile (Fig. 2). If FD reflections are absent or are significantly lower than the statistical (random) noise, the neutron count at each 2θ is distributed according to the Poisson statistics, originating from the counting process of radiation quanta [21]. The observed I_+ and I_- (not shown) at each 2θ were $\sim 10^4$ neutron counts. Hence, the Poisson distribution converges to normal (Gaussian) distribution, with standard deviations of $(I_+)^{1/2}$ and $(I_-)^{1/2}$ for I_+ and I_-, respectively [21]. In this case (absence of FD reflections), X [Eq. (1)] at each 2θ, is a random number and its distribution over 2θ (Fig. 2) should yield an average $\langle X \rangle = 0$ and a standard deviation $(\langle X^2 \rangle - \langle X \rangle^2)^{1/2} = 1$ [21]:

$$X \equiv \frac{I_+ - I_-}{\sqrt{I_+ + I_-}} \tag{1}$$

The frequency [21] distribution of X, extracted from the observed FD profile at 10 K (Fig. 2), is presented in Fig. 6 with a Gaussian curve best fit.

The obtained average and standard deviation of X (Fig. 6), which are 0.01(2) and 0.98(3), respectively, agree (within their respective precision) with those expected from a pure random distribution. This result excludes the existence (within precision) of any nonrandom contribution (e.g., magnetic Bragg reflections) in the observed FD profile. Hence, either no LRO is present or the magnitude of the ordered magnetic moments is smaller than the VIP diffractometer's sensitivity limit.

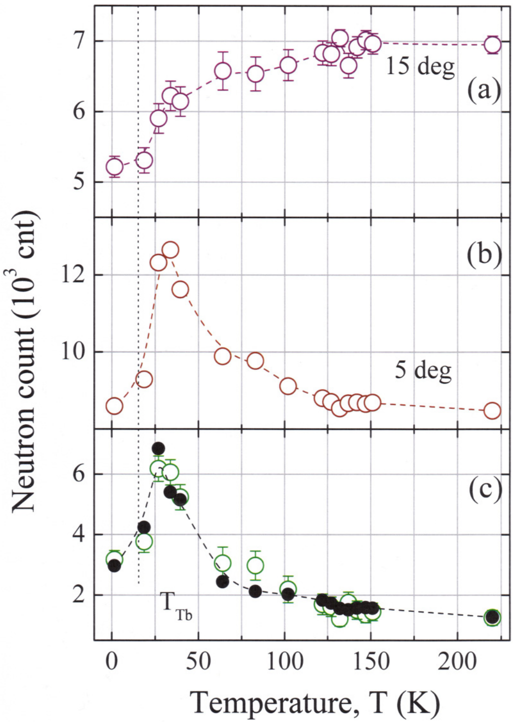

FIG. 5. (Color online) Temperature evolutions of (a) the neutron count at $2\theta = 15°$, which corresponds to the nuclear incoherent scattering and the paramagnetic scattering; (b) the neutron count at $2\theta = 5°$, small-angle scattering, which corresponds (see text) to paramagnetic scattering and MDS; and (c) the small-angle MDS contribution, obtained from (b) − (a) (open circles). The MDS term (solid circles) is calculated [Eq. (2)] using the refined B and ζ values (Table I, see text). The dashed lines are guides to the eye. Where not shown, the error bars are smaller than the symbol's size.

2. *Sensitivity limit of VIP*

Consider the sensitivity or the detection limit of the VIP diffractometer for an ordered magnetic moment located on the $3g$ site (Fig. 1). This sensitivity depends on the neutron flux, detection efficiency, angular resolution, measurement time, total number of unit cells in the sample, and the Bragg FD count (Appendix A). The neutron flux, detection efficiency, and angular resolution of the VIP diffractometer are determined by comparing results of a PNPD experiment performed on $TbCo_2Ni_3$ under similar experimental conditions (Appendix A) [16]. Using the calculated FD count for different magnitudes of the ordered magnetic moment on the $3g$ site, it is found that the sensitivity limit is ~0.05, 0.02, and 0.03 μ_B for a magnetic axis parallel to c, a magnetic axis perpendicular to c, and a soft magnetic material, respectively (Appendix A).

B. $TbCo_3B_2$ NPD study

1. *Generalized three-component Rietveld refinement*

The observed profile broadening (Fig. 3) and its temperature evolution (Fig. 4) originate from a contribution of MDS, which can result from magnetic SRO. Thus, we reanalyze the NPD data, including the MDS, in addition to the Bragg contributions. The expected neutron count I for LRO and SRO scattering as a function of the momentum transfer q relative to the momentum transfer, which corresponds to a Bragg reflection τ, is [22–24]

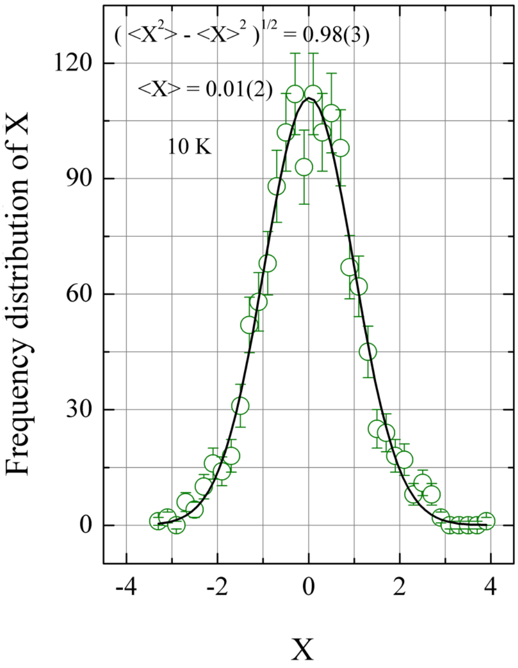

FIG. 6. (Color online) Frequency distribution of X [circles, Eq. (1)], obtained using the YCo_3B_2 FD profile at 10 K (Fig. 2). An error-sensitive fitting procedure of a Gaussian curve (line) yields average and standard deviation $\langle X\rangle = 0.01(2)$ and $(\langle X^2\rangle - \langle X\rangle^2)^{1/2} = 0.98(3)$, respectively.

$$I(q) = \int \left(A\delta(q - q') + \frac{B}{\pi}\frac{\zeta^{-1}}{(q - q')^2 + \zeta^{-2}} \right) \times R(q') f^2(q - q') dq' \qquad (2)$$

where $A \propto |F_n|^2 + |F_m|^2$ corresponds to the integrated neutron count of the LRO (Bragg) term [20]; F_n is the nuclear structure factor for $TbCo_3B_2$ [3]; $F_m = p\mu_{Tb}$ is the magnetic structure factor of the Tb ($1a$) site, $p \equiv 1/2\gamma r_0 g f(q)$ is the magnetic scattering length [20], $\gamma = 1.913$ is the neutron's gyromagnetic ratio, $r_0 = 2.818$ fm is the classical electron radius, $g = 3/2$ is the Tb^{3+} Lande factor [8], $f(q)$ is the magnetic form factor of the Tb^{3+} ion [8], μ_{Tb} is the magnitude of the ordered (LRO) Tb magnetic moment; $B \propto |F_{SR}|^2$ is the integrated neutron count of the SRO (MDS) term with the same proportionality constant as in A; and $F_{SR} \equiv p\mu_{SR}$, μ_{SR} is a refined parameter (see below); $q \equiv K - \tau$, $K = 4\pi \sin\theta/\lambda$ is the scattering vector, 2θ is the scattering angle, $\lambda = 1.8857(5)$ Å [3] is the incident neutron's wavelength, $\tau = 2\pi/d$ is the reciprocal lattice vector, d is the lattice spacing; ζ is the average range of the magnetic clusters (correlation length); and $R(q)$ is the angular resolution function.

In the present work, $R(q)$ is equal to the instrumental resolution function (finite collimation and nonideal monochromation) [25], modified by the effect of the sample's grain size and microstrains. The instrumental resolution function of the HRPT diffractometer is obtained using NPD Rietveld analysis of a $Na_2Al_2Ca_3F_{14}$ standard [26,27]. The effect of microstrain and finite size of the powder grains is found using the Rietveld refinement of the 298 K NPD profile, assuming that MDS in this temperature is negligible. This assumption is then confirmed by analysis (Fig. 4). While microstrains are found to be absent, the typical size of the powder grains, ∼0.10(5) μm, generates a Lorentzian line broadening of the Bragg reflections [28]. A Gaussian line broadening component, which may also appear due to the grains size [28,29], was considered and found negligible.

The MDS originates from clusters of magnetically aligned moments (SRO), which fluctuate over time. If present, antiferromagnetic SRO does not conform with the crystal structure and requires the appearance of neutron count in the vicinity of new Bragg reflections that are additional to those contributed by the crystal lattice. Because no additional reflections were observed [3], we conclude that only ferromagnetic SRO is present. Because the range of these clusters is small compared to the grain's size, the reflections from them are broadened compared to Bragg reflections [20,28]. Assuming that the SRO is isotropic (i.e., the orientation of the cluster's magnetic moment in the grain is random), the angular profile contributed by MDS in the vicinity of the Bragg reflections is a Lorentzian [second term in Eq. (2)] to a first approximation in $q\zeta$ [28,30].

The MDS in the observed NPD profile (Fig. 4) is accounted for in a generalized, three-component Rietveld analysis [Eq. (2)]. The three components are nuclear Bragg (LRO), magnetic Bragg (LRO), and magnetic diffuse (SRO). The nuclear and magnetic Bragg components are included in the first term [Eq. (2)], and the sum of their contributions is equal to A. The third component is included in the second term, and its contribution is equal to B. The grain size feature, with the Lorentzian profile contribution offered by the FullProf program [29], is used in the refinement of the third component, with ζ playing the role of the refined grain size at each NPD temperature. The refined parameter Y [29] is related to ζ through the Scherrer [31] equation. In addition a magnetic moment, μ_{SR}, related to B [Eq. (3)] is refined at each NPD temperature. The pseudo-Voigt angular profile function [29,32] offers an adequate representation of the three-component profile [Eq. (2)].

It follows from the definitions of A and B [Eq. (2)] that the following relation holds for B in the generalized three-component refinement:

$$B = A\frac{p^2\mu_{\mathrm{SR}}^2}{|F_{\mathrm{n}}|^2 + p^2\mu_{\mathrm{Tb}}^2} \tag{3}$$

The refined values of A, B, ζ/ζ_0, μ_{Tb} (present paper), and $\mu_{\mathrm{Tb}'}$ (previous paper [3]) are presented in Table I, where $\zeta_0 = 65(25)$ Å is the minimum value of ζ obtained at 39.4 K.

In addition to the three-component Rietveld refinement, a second technique was used (Appendix B), in which A and (B, ζ) were separately and iteratively refined so that the calculated [Eq. (2)] profile will best fit the observed profile. The A, B, and ζ thus obtained were found to agree, within their uncertainties, with those obtained using the generalized three-component refinement (Table I). Using agreement requirement between the two methods, a systematic uncertainty roughly equal in size to the propagated (one standard deviation) experimental uncertainty, which originates from correlation among the fitted A, B, and ζ, was estimated and added to the total error values (one standard deviation) in Table I.

TABLE I. Refined values of the magnetic parameters of $\mathrm{TbCo_3B_2}$. The parameters A, B, and ζ, are defined in Eq. (2). $\zeta_0 = 65(25)$ Å is the minimum value of ζ. μ_{Tb} and $\mu_{\mathrm{Tb}'}$ are, respectively, the three components (present paper) and two components (previous paper [3]) refined Tb magnetic moments. Numbers in parentheses represent the standard deviation of the last significant digit. "*" denotes value is missing due to no convergence of the fitting procedure. "–" denotes values were not previously reported [3].

T (K)	A (10^3cnt)	B (10^3cnt)	ζ/ζ_0	μ_{Tb} (μ_{B})	$\mu_{\mathrm{Tb}'}$ (μ_{B})
1.53(3)	51(4)	11(3)	2.8(1)	4.8(2)	5.2(1)
18.6(2)	43(6)	12(3)	2.0(1)	4.3(3)	4.8(1)
26.9(1)	9(3)	13(3)	1.2(2)	2.0(3)	2.4(1)
33.7(3)	0.14(2)	9.2(5)	1.06(6)	0.0(2)	0.88(1)
39.4(1)	0.16(2)	8.3(4)	1.00(5)	0.1(1)	0.83(1)
64.0(4)	0.12(2)	4.5(5)	1.35(6)	− 0.1(1)	0.62(1)
82(1)	0.16(2)	3.9(6)	1.42(5)	0.1(1)	0.48(2)
102(1)	0.23(3)	3.3(6)	1.26(5)	0.2(1)	0.43(2)
122(2)	0.16(2)	2.8(5)	1.20(5)	0.1(1)	0.34(2)
127(1)	0.14(2)	2.8(5)	1.31(6)	0.1(1)	–
132(1)	0.12(2)	2.3(5)	1.3(1)	0.1(1)	–
137(1)	0.14(2)	2.3(5)	1.32(6)	0.0(1)	0.33(2)
142(1)	0.14(2)	2.3(6)	1.20(6)	− 0.1(1)	0.29(2)
147(1)	0.14(2)	2.3(6)	1.2(1)	− 0.1(1)	–
151(1)	0.14(2)	2.2(7)	1.2(1)	0.0(1)	0.26(2)
220(1)	0.14(2)	1.4(9)	1.1(2)	0.00(5)	0
298(1)	0.14(2)	0.2(2)	*	0.00(5)	0

2. *LRO and magnetic structure*

Below T_{Tb}, the revised μ_{Tb} values—i.e., those refined with MDS as a third component (present paper)—are slightly lower than $\mu_{\mathrm{Tb}'}$ refined with MDS included in the second component (previous [3] paper). However, above T_{Tb}, the refined μ_{Tb} values are practically zero (Table I and Fig. 7)—unlike $\mu_{\mathrm{Tb}'}$, whose values increase monotonically from 0.26 μ_{B} at 151 K to 0.88 μ_{B} at 33.7 K [3]. In addition, the revised low-temperature orientation (not shown) of μ_{Tb} is perpendicular to the hexagonal c axis. This orientation is in agreement with anisotropy calculations based on induced magnetic transition theory [8], whereas the orientation of $\mu_{\mathrm{Tb}'}$ was reported (previous paper [3]) to be 74(2)° with respect to the c axis.

3. *SRO and correlation length*

The temperature evolution of ζ should be discussed in the following context: SRO results from an equilibrium between fluctuating MEFs, which create regions of aligned magnetic moments, and temperature, which drives to random magnetic moment orientations and magnitude (entropy) [28].

The temperature evolution of ζ, relative to its minimum value $\zeta_0 = 65(25)$ Å (Table I), is presented in Fig. 8. Three temperature regions are identified: $T_\Delta < T$, $T_{\mathrm{Tb}} < T < T_\Delta$, and $T < T_{\mathrm{Tb}}$, where $T_\Delta = 63$ K (Sec. IV). At high and low temperatures ($T_\Delta < T$ and $T < T_{\mathrm{Tb}}$, respectively), the evolution of ζ/ζ_0 (Fig. 8) follows theoretical prediction (Sec. IV) and those reported [22,34,35] in other papers. In the second region,

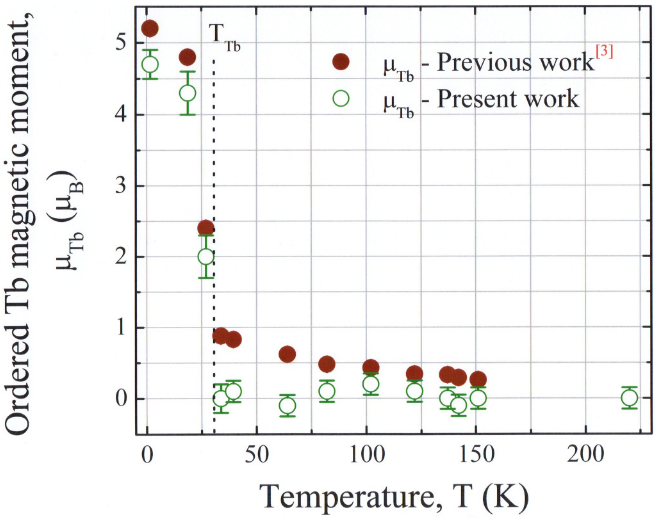

FIG. 7. (Color online) Temperature evolution of the refined ordered magnetic moment μ_{Tb}. Previous paper [3]: MDS was included in the second component (magnetic Bragg) in the refinement (solid circles). Present paper: MDS is included as a third component, dominated by a Lorentzian line shape, in the refinement (open circles). If not shown, the error bars are smaller than the symbol's size.

$T_{\mathrm{Tb}} < T < T_{\Delta}$, anomalous evolution is observed (Fig. 8). This anomaly, and its relation to the magnetic state of Tb ions in $\mathrm{TbCo_3B_2}$, is discussed in Sec. IV.

A large systematic uncertainty of ~30% in the absolute ζ values is contributed by $R(q)$. However, ζ/ζ_0 is only weakly affected by this uncertainty and is dominated by statistical errors (Fig. 8).

4. Small-angle scattering

MDS also contributes to the neutron count in the vicinity of the forward ($2\theta = 0$) scattering direction (critical magnetic scattering) [28]. Hence, the neutron count at small 2θ is the sum of nuclear incoherent scattering, constant (negligible in comparison to the other contributions) neutron background, paramagnetic scattering, and MDS. Neglecting the change in $f^2(q)$ for $\mathrm{Tb^{3+}}$ between 5° and 15° (smaller than 5%) [8], the observed neutron count of the aforementioned first three contributions at 15° [Fig. 5(a)] equals that at 5° [Fig. 5(b)]. Hence, the forward direction MDS is obtained by subtracting the neutron count obtained at 15° from that obtained at 5°. The 5° observed MDS temperature evolution thus obtained is shown (open circles) in Fig. 5(c). This MDS contribution corresponds to the second term in Eq. (2). We calculate this term using refined values of B and ζ (Table I) at $q = 0.291$ Å^{-1} ($2\theta = 5°$) at each temperature (Table I). The values thus obtained are also shown (solid circles) in Fig. 5(c). The agreement with the observed MDS temperature evolution at $2\theta = 5°$ corroborates the results (B and ζ) of our MDS analysis near the (100) reflection at $2\theta \sim 25°$.

IV. DISCUSSION

The result of the present paper, namely, no Co LRO in $R\mathrm{Co_3B_2}$ (R = Tb, Y), allows us to state the following: Tb orders magnetically in $\mathrm{TbCo_5}$ [36], $\mathrm{TbCo_4B}$ [37], $\mathrm{TbCo_3B_2}$, and $\mathrm{TbCo_2Ni_3}$ [16], while Co orders with the Tb whenever it orders in the corresponding Y compound. This ordering occurs when Co occupies (all or part of) the $2c$ site. This site has a uniaxial symmetry $\bar{6}m2$ ($\bar{6}$ along the c axis, Fig. 1) and a strong magnetocrystalline anisotropy (MCA), with the soft direction along the c axis. This MCA is responsible for the c axis magnetism at high temperatures in the $R\mathrm{Co_5}$ compounds [7]. In addition, the absence of Co LRO (i.e., the absence of a localized ordered magnetic sublattice) in $\mathrm{YCo_3B_2}$ supports the itinerant, exchange enhanced, paramagnetic nature suggested by Burzo *et al.* [14] for the Co occupying the $3g$ site.

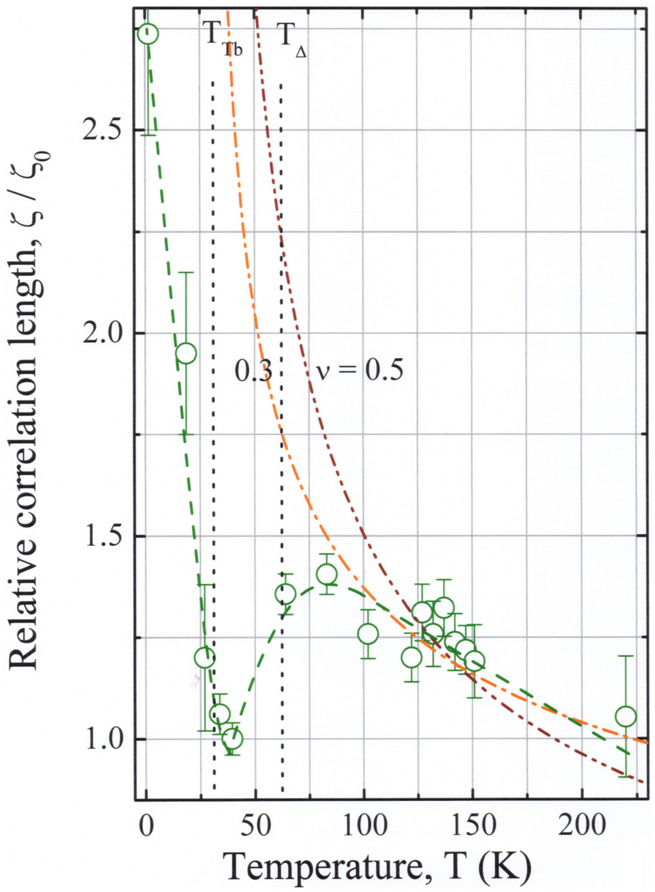

FIG. 8. (Color online) The temperature evolution of the correlation length relative to its minimum value $\zeta_0 = 65(25)$ Å (circles, Table I). T_{Tb} and T_{Δ} correspond to the temperatures of the ordering and of the first excited state [8] of the Tb ions, respectively (see text). In addition, the expected temperature evolutions for $T_{\mathrm{Tb}} < T$, according to the MEF theory [33] and using the critical exponents (Sec. IV) $\nu = 0.3$ (dashed-dotted) and $\nu = 0.5$ (dashed-double dotted), are presented. The dashed line, which connects the circles, is a guide to the eye.

SRO (that is, aligned Tb magnetic moment clusters) is found in the ferromagnetic and paramagnetic temperature regions of $\mathrm{TbCo_3B_2}$. In the paramagnetic region, the SRO extends well above the magnetic ordering temperature T_{Tb} and vanishes only above $T/T_{\mathrm{Tb}} \sim 7$. We suggest that the existence of a nonmagnetic singlet ground state, well separated from the first excited state by an energy gap $\Delta = 5.5(5)$ meV [8] that corresponds to $T_\Delta = 63(5)$ K (Fig. 8), leads to rapidly fluctuating MEFs. The magnitude of this energy gap compared to the energy associated with the MEF, $\mu_B H_m$, is estimated as $\Delta/\mu_B H_m \approx 10$ [8]. These fluctuating MEFs create clusters of Tb ions with partially admixed [8] levels, which tend to align (SRO). Above $T_{\rm Tb}$, the rate of de-excitation (back to the nonmagnetic ground state) that causes the clusters to vanish is greater than that of the admixture, and magnetic LRO is not sustainable.

The isotropic MEF theory [33] predicts the temperature evolution of the correlation length to be $\zeta \propto (T - T_C)^{-\nu}$, where T_C is the ordering temperature and ν is the critical exponent. $\nu = 0.5$, 0.63, 0.71, and 1 for isotropic, three-dimensional (3D) Heisenberg, 3D Ising, and 2D Ising ferromagnets, respectively. The temperature evolution of ζ deduced in the present paper (Fig. 8) approximately follows, at high temperatures ($T_\Delta < T$) the predicted evolution with $\nu \sim 0.3$. However, a strong anomaly is observed at lower temperatures ($T < T_\Delta$). This anomaly is caused by the increase (upon cooling) in the thermal occupancy of the nonmagnetic singlet ground state. This decreases the admixture of excited magnetic states [8] and, in turn, decreases (upon cooling) the extent (i.e., correlation length) of the magnetic clusters. At low temperatures ($T < T_{\rm Tb}$), the ground state turns magnetic, causing this trend to reverse and follow the predicted [33] evolution (though with a considerable shift).

V. CONCLUSIONS

Polarized neutron diffraction confirmed that the Co sublattice in materials derived from RCo$_5$ (R = Tb, Y) orders ferromagnetically [7,38,39] when Co occupies part of the $2c$ site. In RCo$_3$B$_2$, the complete occupancy of the $2c$ site by B leads to a nonmagnetic Co sublattice. This finding supports the itinerant magnetic nature proposed by Burzo *et al.* [14] for the Co at the $3g$ site.

The neutron counts in excess of those contributed by the crystal (nuclear scattering) found in NPD of TbCo$_3$B$_2$ in the paramagnetic region consists of MDS, contributed by the Tb SRO. After this MDS contribution is correctly introduced into the analysis, the resulting revised magnetic structure contains (i) no Co ordering at all temperatures, in agreement with the aforementioned nonmagnetism of the $3g$ site, (ii) above $T_{\rm Tb}$, only short-range magnetic ordering of the Tb ions, (iii) below $T_{\rm Tb}$, ferromagnetism of the Tb with the magnetic axis perpendicular to the hexagonal axis, in agreement with anisotropy calculations [8].

The emergence of SRO in this singlet ground state system is driven by the mechanism of induced ordering (Sec. I) [8,13]. Consequently, the temperature evolution of the correlation length for this SRO in the paramagnetic region is fundamentally different from that predicted by isotropic MEF [29] theory.

ACKNOWLEDGMENT

This paper is partially based on Experiment No. 10573, performed at the Orpheé research reactor in the Laboratoire Léon Brillouin, CEA-CNRS, Saclay, France.

APPENDIX A: VIP DIFFRACTOMETER DETECTION LIMIT

The VIP diffractometer detection limit (sensitivity) for an ordered Co sublattice at the $3g$ site (Fig. 1) depends on the instrumental scale factor [25] L [Eq. (A1)] and angular resolution R [Eq. (2)].

The value of L is extracted from the refinement of the magnetic parameters of TbCo$_2$Ni$_3$ [16], which fits the calculated FD, $I_+ - I_-$ [Eq. (A1)], to the observed integrated FD count [40] for the 101 reflection. The extracted value is $L = 200$ integrated neutron counts per hour of irradiation per mole of unit cells in the powder sample:

$$I_+ - I_- = L N_c t D(2\theta) T(2\theta) \langle \cos\beta \rangle_{\rm hkl} \times \frac{e^{-2B_T \sin^2\theta/\lambda^2}}{\sin\theta \sin 2\theta} m_{\rm hkl} {\rm Re}\{F_N F_M^\dagger\} \qquad (A1)$$

where N_c is the number of unit cell moles in the sample, t is the irradiation time (in hours), $D(2\theta)$ is the beam depolarization inside the sample, $T(2\theta)$ is the absorption corrected geometrical transmission function (in Debye-Scherrer's geometry), $\langle \cos\beta \rangle_{\rm hkl}$ [40] is the fractional domain magnetization in the externally applied magnetic field averaged over the grains contributing to reflection hkl, and the other notations have their usual [40] meanings.

The PNPD was shown to be highly sensitive to the anisotropy of the investigated magnetic structure [40,41]. We simulate a FD profile from LRO Co in YCo$_3$B$_2$ with $\mu_{\rm Co} = 0.05$ μ_B. Three MCA models (Fig. 9) are considered: soft magnetic structure, hard magnetic structure with the easy direction perpendicular to the hexagonal c axis, and hard magnetic structure with the easy direction parallel to the hexagonal c axis. For the soft magnetic structure, $\langle \cos\beta \rangle_{\rm hkl} = 1$ [40]. For hard uniaxial magnetic materials in which the magnetic axis is

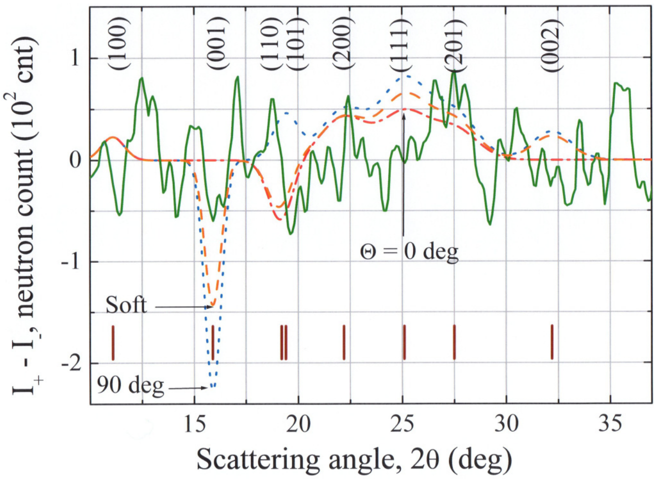

FIG. 9. (Color online) The observed (solid line, 10 K) and calculated (see text) FD profiles, $I_+ - I_-$, for YCo$_3$B$_2$, assuming an ordered moment of 0.05 μ_B at the $3g$ site. Three models for the Co MCA are considered: soft (dashed line), hard oriented parallel (dotted line), and hard oriented perpendicular (dashed-dotted line) to the hexagonal c axis. The expected reflections 2θ positions are marked, and their Miller ($P6/mmm$) indices are given.

oriented with an inclination angle Θ with respect to the unique axis, $\langle \cos\beta \rangle_{\mathrm{hkl}}$ is [40]

$$\langle \cos\beta \rangle_{\mathrm{hkl}} = \frac{2}{\pi} (\cos\Theta \sin\alpha_{\mathrm{hkl}} + \sin\Theta E(\pi/2 - \alpha_{\mathrm{hkl}})) \tag{A2}$$

where α_{hkl} is the angle between the magnetic moment and the direction of the hkl reflecting planes and $E(\pi/2 - \alpha_{\mathrm{hkl}})$ is the complete elliptic integral of the second kind [40].

The FD integrated neutron count for the hkl reflections (Fig. 2) are calculated using Eqs. (A1) and (A2), the irradiation time t of ~50 h (at 10 K), and the number of unit cells in the $\mathrm{YCo_3B_2}$ powder sample N_c ~0.035 moles. Using VIP [16] angular resolution, these calculated integrated neutron counts are converted back to FD profiles. The profiles thus obtained for soft (dashed line); hard, oriented parallel (dashed-dotted line); and perpendicular (dotted line) to the hexagonal c axis, are shown in Fig. 9.

Let us adopt the criterion that the sensitivity limit is achieved when the amplitude of a FD reflection becomes about equal to the amplitude in a strong fluctuation of the FD background noise (~75 cnt, Fig. 9). Using the three calculated profiles for $\mu_{\mathrm{Co}} = 0.05\ \mu_{\mathrm{B}}$ (Fig. 9) and the amplitude of a FD reflection being proportional to μ [Eq. (A1)], we obtain the following sensitivity limits: μ_{Co} ~0.05, 0.02, and 0.03 μ_{B} for the magnetic axis parallel to c, magnetic axis perpendicular to c, and soft magnetic material, respectively.

APPENDIX B: THE SEPARATE LRO SRO ANALYSIS PROCESS

The proposed fitting procedure is based on two Bragg component Rietveld refinement (nuclear and magnetic LRO) and a least-squares (LS) minimization procedure [27] that fits the MDS to a Lorentz profile. The two procedures are applied sequentially by iterations until the sum of the Rietveld (Bragg) and the LS (MDS) profiles gives a good fit to the observed profile.

This procedure includes four steps that are repeated iteratively: (i) the LRO component $A^{(1)}$ is refined using the two-component Rietveld refinement (whole NPD profile fit); (ii) the angular LRO profile, calculated using this $A^{(1)}$, is subtracted from the observed profile, revealing the MDS contribution; (iii) $B^{(1)}$ and $\zeta^{(1)}$ are refined to fit this MDS contribution using the LS process; (iv) the angular SRO profile, calculated using $B^{(1)}$ and $\zeta^{(1)}$, is subtracted from the observed profile, revealing the Bragg profile. The $A^{(2)}$ is refined to fit this Bragg profile in a manner similar to step (i). This procedure is repeated until the change in iteration j, between $A^{(\mathrm{j}+1)}$, $B^{(\mathrm{j}+1)}$ and $A^{(\mathrm{j})}$, $B^{(\mathrm{j})}$ is smaller than the experimental precision of the observed integrated neutron count.

[1] Th. Hahn (ed.), *International Tables for Crystallography: Space-Group Symmetry*, (Kluwer, Dordrecht, the Netherlands, 1995), Vol. A.

[2] E. A. Nesbitt and J. H. Wernick, *Rare Earth Permanent Magnets* (Academic Press, New York, 1973).

[3] M. Dubman, E. N. Caspi, H. Ettedgui, L. Keller, M. Melamud, and H. Shaked, Phys. Rev. B **72**, 024446 (2005).

[4] E. Wolfson, E. N. Caspi, H. Ettedgui, H. Shaked, and M. Avdeev, J. Phys. Condens. Matter **22**, 026001 (2010).

[5] O. Sigalov, A. I. Shames, E. N. Caspi, M. Dubman, H. Ettedgui, S. D. Goren, and H. Shaked, J. Appl. Phys. **98**, 074105 (2005).

[6] C. Chacon and O. Isnard, J. Phys. Condens. Matter **13**, 5841 (2001).

[7] Z. Tie-song, J. Han-min, G. Guang-hua, H. Xiu-feng, and C. Hong, Phys. Rev. B **43**, 8593 (1991).

[8] O. Rivin, R. Osborn, A. I. Kolesnikov, E. N. Caspi, and H. Shaked, Phys. Rev. B **78**, 184424 (2008).

[9] H. Yamada, K. Terao, H. Nakazawa, I. Kitagawa, N. Suzuki, and H. Ido, J. Magn. Magn. Mater. **183**, 94 (1998).

[10] R. J. Radwanski, J. Magn. Magn. Mater. **62**, 120 (1986).

[11] B. Bleaney, Proc. R. Soc. A **276**, 19 (1963).

[12] G. T. Trammell, Phys. Rev. **131**, 932 (1963).

[13] B. R. Cooper and O. Vogt, J. Phys. Paris **32**, 958 (1971).

[14] E. Burzo, P. Vlaic, V. Pop, and I. Creanga, J. Optoelectron. Adv. Mater. **8**, 484 (2006).

[15] A. Gukasov, S. Rodrigues, J. L. Meuriot, T. Robillard, A. Sazonov, B. Gillon, A. Laverdunt, F. Prunes, and F. Coneggo, Phys. Procedia **42**, 150 (2013).

[16] O. Rivin, E. N. Caspi, H. Ettedgui, H. Shaked, and A. Gukasov, Phys. Rev. B **88**, 054430 (2013).

[17] A. Delapalme, J. Schweizer, G. Couderchon, and R. P. de la Bathie, Nucl. Instrum. Meth. **95**, 589 (1971).

[18] M. Potter, H. Fritzsche, D. H. Ryan, and L. M. D. Cranswiek, J. Appl. Cryst. **40**, 489 (1978).

[19] A. Gukasov and P. J. Brown, J. Phys. Condens. Matter **22**, 502201 (2010).

[20] G. E. Bacon, *Neutron Diffraction*, 3rd ed. (Clarendon Press, Oxford, UK, 1975).

[21] B. P. Roe, *Probability and Statistics in Experimental Physics* (Springer-Verlag, New York, 1992).

[22] A. K. Bera, S. M. Yusuf, and I. Mirebeau, J. Phys. Condens. Matter **23**, 426005 (2011).

[23] S. M. Shapiro, G. Aeppli, H. Maletta, and K. Motoya, Phys. B **137**, 96 (1986).

[24] W. Tian, A. Kreyssig, J. L. Zarestky, L. Tan, S. Nandi, A. I. Goldman, T. A. Lograsso, D. L. Schlagel, K. A. Gschneidner, V. K. Pecharsky, and R. J. McQueeney, Phys. Rev. B **80**, 134422 (2009).

[25] B. T. M. Willis, *Thermal Neutron Scattering* (University Press, Oxford, UK, 1970).

[26] M. V. Lobanov, M. Greenblatt, E. N. Caspi, J. D. Jorgensen, D. V. Sheptyakov, B. H. Toby, C. E. Botez, and P. W. Stephens, J. Phys. Condens. Matter **16**, 5339 (2004).

[27] S. Heiroth, *Pulsed Laser Deposition of Functional Electroceramic Thin Films for Micro Solid Oxide Fuel Cell Applications*, Sc.D. Diss. (ETH Zurich, Basel, 2010), http://e-collection.library.ethz.ch/eserv/eth:1460/eth-1460-02.pdf.

[28] P. A. Egelstaff, *Thermal Neutron Scattering* (Academic Press, London, 1965).

[29] J. R. Carvajal, *An Introduction to the Program Fullprof 2000*, http://www.ill.eu/sites/fullprof/php/tutorials.html.

[30] I. A. Zaliznyak and S. H. Lee, *Magnetic Neutron Scattering*, http://neutrons.phys.bnl.gov/presentations/MagneticNeutronScattering_proofed_indexed_unlined.pdf.

[31] The Scherrer equation $\zeta = 0.89\lambda/\mathrm{Y}$, where Y is the grain's size parameter in the Fullprof [26] software.

[32] NPR = 7.

[33] D. C. Mattis, *The Theory of Magnetism Made Simple* (World Scientific Publishing, Singapore, 2006).

[34] M. J. Cooper and R. Nathans, J. Appl. Phys. **37**, 1041 (1966).

[35] R. D. Lowde, Rev. Mod. Phys. **30**, 69 (1958).

[36] T. Okamoto, H. Fujii, C. Inoue, and E. Tatsumoto, J. Phys. Soc. Jpn. **34**, 835 (1973).

[37] E. N. Caspi, M. Dubman, H. Ettedgui, H. Shaked, M. Melamud, L. Keller, and M. Avdeev, Phys. B **385**, 339 (2006).

[38] K. H. J. Buschow, M. Brouha, J. W. M. Biestrerbos, and A. G. Dirks, Phys. B **91**, 261 (1977).

[39] A. Haldar, I. Dhiman, A. Das, K. G. Suresh, and A. K. Nigam, J. Alloys Comp. **509**, 3760 (2011).

[40] O. Rivin, H. Shaked, A. Gukasov, and E. N. Caspi, J. Neut. Res. (2014) (to be published).

[41] R. M. Moon, T. Riste, and C. Koehler, Phys. Rev. **181**, 920 (1969).